Geoscience Frontiers 16 (2025) 101962

Contents lists available at ScienceDirect

Geoscience Frontiers

journal homepage: www.elsevier.com/locate/gsf

Research Paper

# Magmatic initial and saturated water thresholds determine copper endowments: Insights from apatite F-Cl-OH compositions

Yingcai Sun [a], Qiushi Zhou [a], Rui Wang [a,b,c,*], Madeleine C.S. Humphreys [d]

[a] State Key Laboratory of Geological Processes and Mineral Resources, Frontiers Science Center for Deep-time Digital Earth, Institute of Earth Sciences, China University of Geosciences, Beijing 100083, China

[b] Hunan Key Laboratory of Rare Metal Minerals Exploitation and Geological Disposal of Wastes, and School of Resources Environment and Safety Engineering, University of South China, Hengyang 421001, China

[c] SinoProbe Laboratory of Chinese Academy of Geological Sciences, Beijing 100037, China

[d] Department of Earth Sciences, Durham University, Science Labs, Stockton Road, Durham DH1 3LE, UK

ARTICLE INFO

*Article history:*
Received 12 July 2024
Revised 18 September 2024
Accepted 8 November 2024
Available online 9 November 2024
Handling Editor: K. Szilas

*Keywords:*
Porphyry copper deposit
Magmatic water threshold
Apatite
Gangdese belt

ABSTRACT

Magmatic volatiles ($H_2O$, F, Cl), especially water, are critical in the formation of porphyry copper deposit, for its significance as a carrier for metals. However, accurately quantifying the water contents of deep ore-forming magma remain a challenge. Here, we used apatite and forward modelling methods to reconstruct magmatic water evolution histories, with special concern on the control of initial magmatic $H_2O$ contents and water saturation threshold to porphyry mineralization. Samples investigated include granitoid rocks and apatite from highly copper-mineralized and barren localities. Generally, our research suggested that both ore-related and ore-barren magma systems are hydrous, the modeled magmatic water contents vary significantly among systems whether mineralized or not, and the major difference lies in the threshold of water saturation (6.0 wt.% for barren, and up to 10.0 wt.% for highly mineralized). Combined with whole rock geochemistry data (high $K_2O$ and Sr/Y contents) and modeling result (high modeled water thresholds), we think the ore-related magmas are stored at deeper depth with higher water solubility. In conclusion, we propose that the level of magmatic water saturation plays a crucial role in the formation of porphyry copper systems. Fertile magma has higher water solubility to which deeper storage depth is a critical contributing factor, and can get significantly water enriched upon saturation.



## 1. Introduction

Water plays an essential role in porphyry copper mineralization (Richards, 2011a; Wang et al., 2014b; Chiaradia, 2020). It acts as a carrier of critical ore-forming components such as copper (Cu), sulfur (S), and chlorine (Cl) (Williams-Jones and Migdisov, 2014). The content of water available in ore-forming magma can be decisive to the eventual metal endowment of porphyry deposits (Richards, 2011b; Chiaradia and Caricchi, 2017). While a "water-rich" condition has been suggested to favor the formation of porphyry copper deposits (Richards, 2011a; Wang et al., 2014a; Chiaradia, 2020), the specific water content required for economic metal endowment remains poorly understood.

Previous researchers have provided qualitative constraints on the water content, based on abundant early amphibole fractionation during differentiation in the mid to deep crust (up to 40 km; Ridolfi et al., 2010) and late-stage plagioclase crystallization at or near volatile saturation in the upper crust, which will result in an elevated Sr/Y ratio (Loucks, 2014). Their studies indicated that the hydrous porphyry ore-forming magmas have a water content above 3.5–4.0 wt.% (Müntener et al., 2001; Richards et al., 2012; Wang et al., 2014a). Lu et al. (2015) proposed that ore-forming magmas have the minimum water content of 10–12 wt.% in southern Tibet. Chiaradia (2020) using systematic modeling proposed that that a water content range of 2 wt.% to 6 wt.% in arc magmas is most conducive to mineralization. Excessively high or low magma water contents are unfavorable for the formation of ore deposits (Chiaradia, 2020). Recent studies indicated that the wetness of ore-forming magma is correlated with its mineralization potential (Huang et al., 2023a,b). However, these studies do not provide a quantitative way to constrain the initial and saturated water thresholds.

* Corresponding author at: State Key Laboratory of Geological Processes and Mineral Resources, Frontiers Science Center for Deep-time Digital Earth, Institute of Earth Sciences, China University of Geosciences, Beijing 100083, China.

*E-mail address:* rw@cugb.edu.cn (R. Wang).

https://doi.org/10.1016/j.gsf.2024.101962
1674-9871/

Quantifying the water content of ore-forming magma, whether in its initial or saturation stages, is a challenging task due to the complexity of ore-forming systems. One of the challenges lies in determining the depth at which the ore-forming magma reaches water saturation. Some studies propose the existence of a large magma chamber at depths of 5–15 km, which branches into smaller plutons at shallow depths of 3–5 km where water saturation occurs (Sillitoe, 2010). On the other hand, other studies suggest that the magma chamber becomes water-saturated at depths greater than 5 km and is emplaced through tectonic uplifting and subaerial erosion (Wang et al., 2024). Therefore, questions remain about the timing of water saturation and how much water is needed to improve the chances of forming a mineralizing system.

To address this issue, we have focused our investigation on a series of porphyry deposits and associated barren granitoids in the Gangdese belt, located in southern Tibet. According to prior studies, some large scale deposits are suggested to contain remarkable amounts of water (>4.5 wt.%, up to 10 wt.% based on whole rock geochemistry and granitic hygrometer; Wang et al., 2014a, b; Lu et al., 2015) Amphibole-dominated fractionation and shovel-like REE distribution patterns of Miocene high Sr/Y granitoids of in the Gangdese belt (Wang et al., 2014a; Yang et al., 2015) all reinforced this viewpoint.

Instead of using whole rock geochemical and crystallization characteristics for estimating water content information, we choose apatite, an accessory mineral with wide stability and capable of recording the volatile contents in magma (Piccoli and Candela, 2002; Webster and Piccoli, 2015), as the tracer of the evolution of magmatic water (Li and Costa, 2020; Humphreys et al., 2021). We selected a set of apatite inclusions in zircons which are less susceptible to alteration processes and have the potential to record historical information of magma (Brenan, 1993; Kendall-Langley et al., 2021). We then use forward simulation based on the MATLAB of Humphreys et al. (2021) to match the natural apatite data and thus better deduce the evolution trajectories of magmatic water and other volatiles. All efforts are aimed to address the problem of how initial and saturated water content plays the role in controlling copper endowment.

## 2. Geological settings

The Himalayan-Tibetan plateau, resulting from Indian-Asian continental collision, is composed of four blocks from south to north: the Himalayas, Lhasa, Qiangtang blocks, and the Songpan-Ganze complex, separated by the Indus-Yarlung Zangbo, Bangong-Nujiang and Jinshajiang sutures, respectively (Fig. 1; Yin and Harrison, 2000; Zhu et al., 2013). Within the Lhasa block, there are three subterranes: the northern, middle, and southern Lhasa subterranes. These subterranes are delineated by two prominent geological features, namely the Shiquanhe River-Nam Tso Mélange zone and the Luobadui-Milashan fault (Fig. 1; Zhu et al., 2011, 2013).

The Gangdese magmatic belt is located in southern Tibet within the Lhasa Block. The northward subduction of the Neo-Tethyan oceanic lithosphere underneath the southern margin of the Lhasa Block produced multi-stage Mesozoic-Cenozoic magmatism along the whole Gangdese belt (Ji et al., 2009). The magmatism of the Gangdese belt is episodic (Zhu et al., 2017), and can be subdivided into five stages (Zhu et al., 2011, 2019). The magmatism of the Indian-Asian post-collision stage is characterized by the emplacement of Miocene high-Sr/Y granitoids (dominating in the east Gangdese belt) and potassic-ultrapotassic (trachytic) volcanic rocks (dominating in the west Gangdese belt)(Wang et al., 2018).

There are three main episodes of porphyry mineralization in the Gangdese belt: Jurassic, Paleocene-Eocene, and Miocene. The most notable mineralization episode is Miocene, including two giant porphyry deposits (Qulong, Jiama) and many intermediate-small porphyry deposits (i.e., Zhunuo, Bangpu, Chongjiang, and Jiru; Yang and Cooke, 2019). These Miocene porphyry deposits are all associated with high-Sr/Y granitoid magmas, which are thought to be oxidized ($\Delta$FMQ = +0.8 to +2.9) and water-rich ($\geq$4 wt.%, up to 10 wt.%; Wang et al., 2014a, b; Lu et al., 2015). Miocene ore-barren adakitic rocks crop out as small volume porphyritic intrusions in the Gangdese belt, (e.g., Kangmaqie, Bangba, Mayum and Yare; Yang et al., 2016).

## 3. Sampling

Zircon grains were manually picked after gravity and magnetic separation, and polished. Euhedral to subhedral magmatic zircon grains without zoning and extensive resorption texture were selected from fresh magmatic rocks. Our zircon-hosted apatite inclusion samples were collected from Miocene Rongmucuola pluton in the Qulong deposit, granodiorite, and granodiorite porphyry in the Jiama deposit, granodiorite in the Jiru deposit, and granite porphyry in Kangmaqie area. Representative BSE images of apatite inclusions in zircon are shown in Fig. 1.

Apatite inclusions in zircon grains are commonly range from 4 to 15 μm and up to 30 μm in length (Fig. 2). The inclusions are euhedral–subhedral and randomly orientated with respect to the crystal growth structure of their host zircon. Apatite inclusions were selected for analysis if they were not associated with cracks or areas of turbid zoning in the host zircon crystal, following the criteria of Bell et al. (2015). Intact magma zircon crystals with apatite inclusions are ubiquitous in most of the ore-related samples, except for the ore-barren suites (several apatite inclusions of Kangmaqie ($n$ = 3) were chosen for EPMA). A total of 61 apatite inclusions were carefully selected from giant deposit (Qulong, Jiama), small deposit (Jiru) and Kangmaqie area.

In addition to newly acquired apatite data (see below), we also compiled published major element data of the Miocene apatite micro-phenocrysts of ore-related magmatic rocks from giant porphyry deposits (Qulong, Jiama) and intermediate to small porphyry deposits (Zhunuo, Chongjiang, Bangpu, Jiru). Details of classified samples are presented in Supplementary Material. We classify these samples into four groups based on their conditions of mineralization: Qulong, Jiama, intermediate-small deposits, and ore-barren suites. By compiling reported data of these categories, we aim to statistically visualize the difference in evolution path of these magmatic systems and try to use forward modeling to reinterpret the natural data.

## 4. Methods

Major and volatile element compositional analyses of apatites were performed at the Nanjing Hongchuang Geological Exploration Technology Service Co. Ltd using a JEOL JXA-iSP100 Electron Probe Microanalyzer, designed by Japan Electronics Corporation. The operating conditions for large apatite inclusions were 15 kV accelerating voltage, 20 nA working current, and 5 μm beam spot diameters. For small apatite inclusions, the operating conditions were 15 kV accelerating voltage, 10 nA working current and 3 μm beam spot diameters. The peak counting time was 10 s for F, Cl and 20 s for S. All EPMA data were then corrected using the ZAF correction method for the matrix effect. The standards were as the follows: Durango Apatite (F, Ca, P), Tugtupite (Cl), Anhydrite (S), Orthoclase (K), Albite (Na), Magnesium (Mg), and Jadeite (Si). In addition, apatite grains were measured on the location perpendicular to their c-axis to further avoid element mobility due to the beam impact (e.g., Goldoff et al., 2012). Detection limits for volatile elements

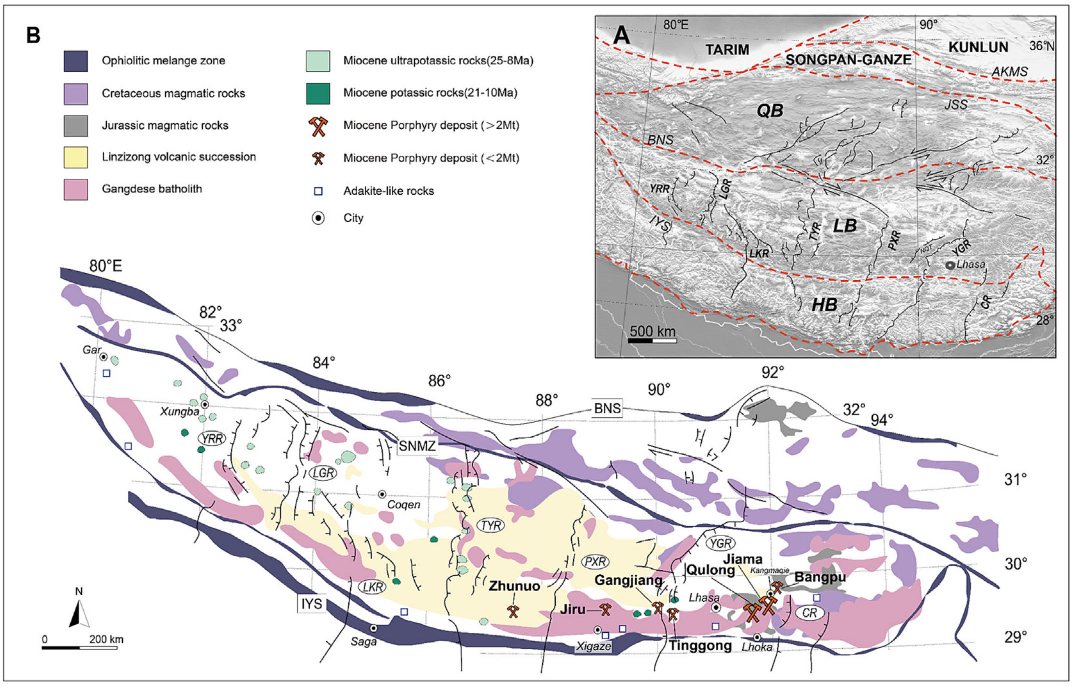


**Fig. 1.** Topographic-geological map of the Gangdese magmatic belt within the Lhasa Block. (A) Map indicating the tectonic framework of the Himalayan-Tibetan orogen with topography and the major block boundaries. Abbreviations: IYS, Indus-Yarlung suture; BNS, Bangong-Nujiang suture; JSS, Jinsha suture; QB, Qiantang block; LB, Lhasa block; HB, Tethyan Himalaya. (B) Simplified geological map of the Lhasa Block (modified after Yang et al., 2016). Abbreviations: YRR, Yari rift; LGR, Lunggar rift; LKR, LopuKangri Rift; TYR, Tangra Yum Co rift; PXR, Pumqu–Xianza rift; YGR, Yadong–Gulu rift; CR, Comei rift; SNMZ, Shiquan River-Nam Tso Mélange.

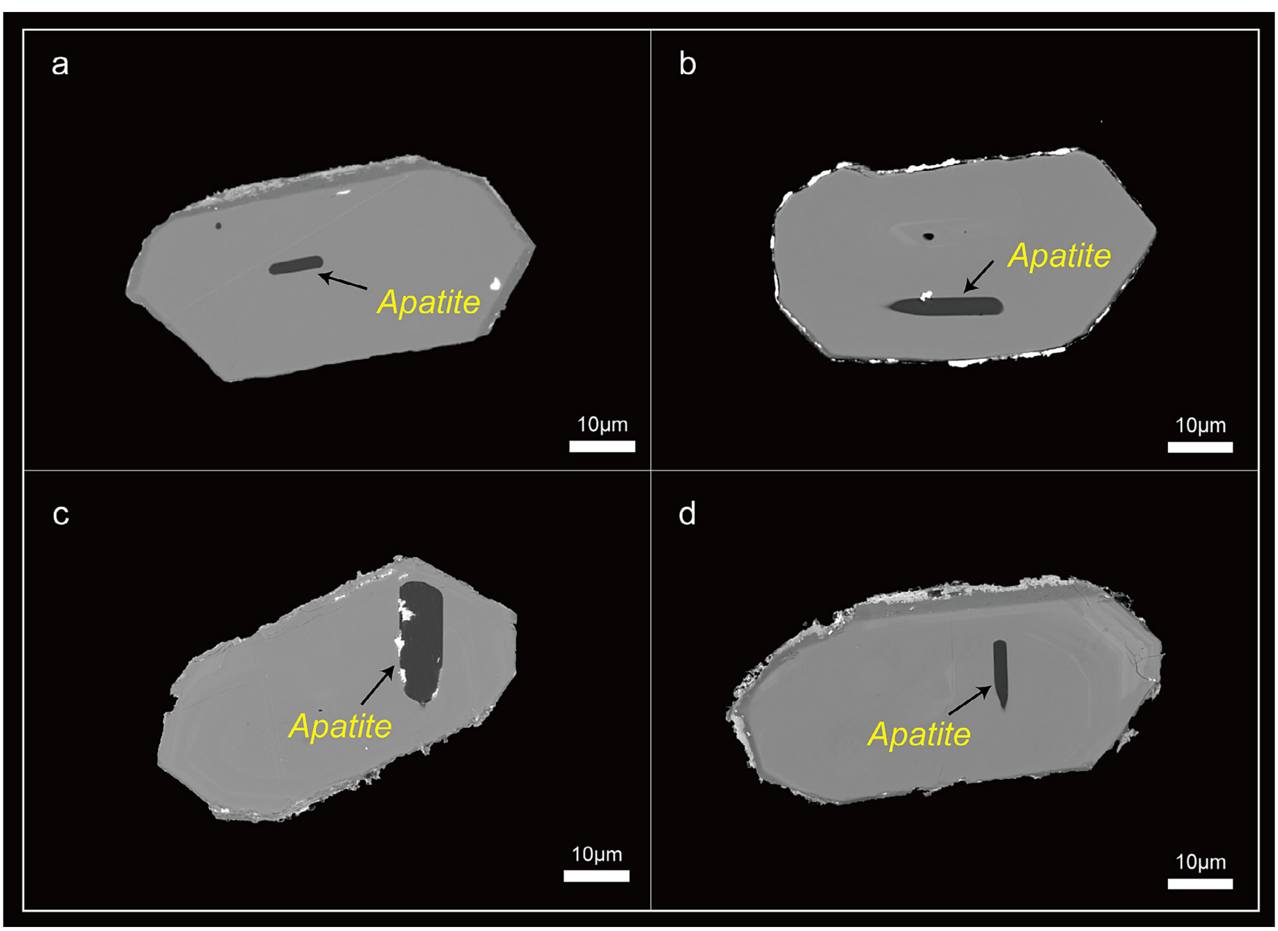


**Fig. 2.** Back-scatter electron (BSE) images of magmatic apatite inclusions in zircon from granodiorite in Qulong deposit (a), granodiorite porphyry in Jiama deposit (b), granodiorite in Jiru deposit (c), and diorite in Kangmaqie (d).

in apatite were typically ~120 ppm for Cl and ~500 ppm for F. The test analysis accuracy of apatite for F and Cl is better than 5%.

## 5. Results

The results of the major and volatile element compositions of apatite are provided in Supplementary Data Table 1. Our analysis reveals that the apatite inclusions exhibit consistently high concentrations of CaO and $P_2O_5$. The CaO content ranges from 51.09 wt.% to 57.66 wt.%, while the $P_2O_5$ content ranges from 38.89 wt.% to 43.95 wt.%. These compositions are indicative of typical magmatic calcium phosphate apatite (Piccoli and Candela, 2002).

To further characterize the apatite compositions, mole fractions of apatite F, Cl, and OH ($X_F$, $X_{Cl}$, and $X_{OH}$) were calculated following the method described by Li and Costa (2020). The composition of most apatite samples falls between the fluorapatite and hydroxyapatite endmembers. The F content shows significant variation, ranging from 1.86 wt.% to 3.67 wt.% (average = 2.79 wt.%), while the Cl content exhibits less variability, ranging from 0.05 wt.% to 0.52 wt.% (average = 0.27 wt.%) (Fig. 3). Notably, there is a strong covariation between $X_{OH}$ and $X_F$, which can be attributed to the very low and weakly variable $X_{Cl}X_{Cl}$. The $X_{OH}$ values were calculated by assuming perfect stoichiometry and using the difference method.

Apatite inclusions in zircon and apatites in the matrix exhibit distinct trends in volatile compositions (Fig. 3). Specifically, the apatite inclusions in the Qulong deposits show higher Cl content (average = 0.63 wt.%, $n$ = 17) and lower F content (average = 2.02 wt.%, $n$ = 17) compared to the matrix apatites (average Cl = 0.28 wt.%; average F = 2.72 wt.%; $n$ = 63) (Fig. 3b). Similarly, the apatite inclusions from the Jiama deposit also have higher Cl content and lower F content (average Cl = 0.34 wt.%; average F = 2.58 wt.%; $n$ = 10) compared to the matrix apatites (average Cl = 0.17 wt.%; average F = 2.95 wt.%; $n$ = 72). Furthermore, the apatite inclusions from the Jiama deposit are spatially arranged along a continuous line (Fig. 3c), which may represent a continuous volatile evolution trajectory of the Jiama deposit.

For the group of intermediate-small deposits, apatite inclusions are collected from the Jiru deposit, while matrix apatites are compiled from the Zhunuo, Chongjiang, Bangpu, and Jiru deposits. In this group, the apatite inclusions have lower Cl (average = 0.18 wt.%, $n$ = 12) and F (average = 2.27 wt.%, $n$ = 12) contents. In contrast, the Cl and F contents of the apatites in the matrix are 0.25 wt.% and 2.80 wt.% on average, respectively. Apatites from the ore-barren suites have high Cl contents (average = 0.42 wt.%, $n$ = 61) and moderate F contents (average = 2.64 wt.%, $n$ = 61). The zircon-hosted apatite inclusions in the ore-barren suites are rare ($n$ = 5) and have average Cl and F contents of 0.27 wt.% and 2.39 wt.%, respectively.

By comparing the volatile compositions of zircon-hosted apatite inclusions and matrix apatites, it is evident that the apatite inclusions in zircon exhibit different volatile trends. This suggests their potential as indicators for tracing the multi-stage changes and characteristics of magmatic volatiles. In this study, a comprehensive dataset of 167 sets of whole rock geochemical data was collected, encompassing Miocene ore-related and ore-barren magmatic rocks from the Gangdese belt (Supplementary Data Table 4). The collected samples represent a range of lithologies, from monzonite to granite, as classified on the TAS diagram (Fig. 4). The $SiO_2$ content of these samples ranges from 58.72 wt.% to 78.75 wt.%, the CaO content ranges from 0.05 wt.% to 5.63 wt.%, and the $K_2O$ content ranges from 1.42 wt.% to 9.51 wt.%. Fig. 4c, d illustrate the variation trend of the whole rock Sr content throughout magma evolution. The ore-related granitic rocks exhibit relatively high Sr contents, reaching up to 1100 ppm, and display a sharp decrease in Sr content (Fig. 4c, d). In contrast, the Sr content of the ore-barren rocks is relatively consistent, with significant overlap with the ore-related rocks in the range of approximately 500–900 ppm.

## 6. Forward modeling based on MATLAB program

Partition coefficients ($D$) are inappropriate to describe the distribution of water and other volatiles between apatite and melt (Stock et al., 2018; Li and Costa, 2020; Humphreys et al., 2021) because multiple volatile ligands (F, Cl and OH) occupy the anion site of apatite. Therefore, the incorporation of any ligand from melt into apatite requires an exchange reaction between the two phases, as defined by the equilibrium constants as a function of pressure and temperature (Li and Costa, 2020; Humphreys et al., 2021). The calculation of $K_d$ needs reliable temperature, and therefore, we compiled Ti-zircon temperature of giant deposits (Qulong and Jiama deposit), intermediate-small deposits and ore-barren samples (e.g., Yang et al., 2015; Wang et al., 2018; Sun et al., 2023a, b), which could reflect the crystallisation condition of apatite inclusions in zircon. Schiller and Finger (2019) suggested that the application of the Ti-zircon temperature in granitic rocks requires further consideration and a constant temperature correction of + 70 °C for almost all S-type and many I-type granites could be more reasonable. The adjusted Ti-zircon temperatures are then used for modelling the bulk crystal-melt partition coefficients are estimated on the basis of mineral assemblage from previous study (e.g., Li and Hermann, 2017; Sun et al., 2018; Wang et al., 2018; Li and Costa, 2020). Volatile-bearing minerals (e.g., amphibole, biotite and apatite) are abundant as phenocrysts, their assemblages are used to calculate bulk rock crystal-melt partition coefficient.

The forward modeling in this study is based on a MATLAB program modified from Humphreys et al. (2021) and described by Lormand et al. (2024). It was designed to reconstruct the evolution of magmatic volatiles by describing the initial and boundary conditions of magma using a series of parameters (for example, initial melt $H_2O$, Cl, F concentration, Tables 1 and 2). The program models the volatile evolution of magma as a function of melt fraction ($F$), considering the separation of a free volatile phase after water saturation (saturation level of water is a preset parameter, equivalent to depth of magma storage). The model calculates the composition of apatite in equilibrium with the evolving melt, which can be matched to the observed natural apatite dataset (Figs. 5 and 6). The range of magmatic conditions are calculated using MATLAB multi-start algorithm and sensitivity analysis are performed to

**Table 1**
Initial parameters used for 'target curve'.

| Type | $D_{fluid–melt}$ | | $K_{OH-H2O}$ | $H_2O$ saturation level (wt.%) |
|---|---|---|---|---|
| | Cl | F | | |
| Qulong deposit | 13 | 1.1 | 0.338 | 10 |
| Jiama deposit | 11 | 1.1 | 0.355 | 10 |
| Intermediate-small deposits | 19 | 1.5 | 0.330 | 7 |
| Ore-barren suites | 16 | 2.0 | 0.300 | 6 |

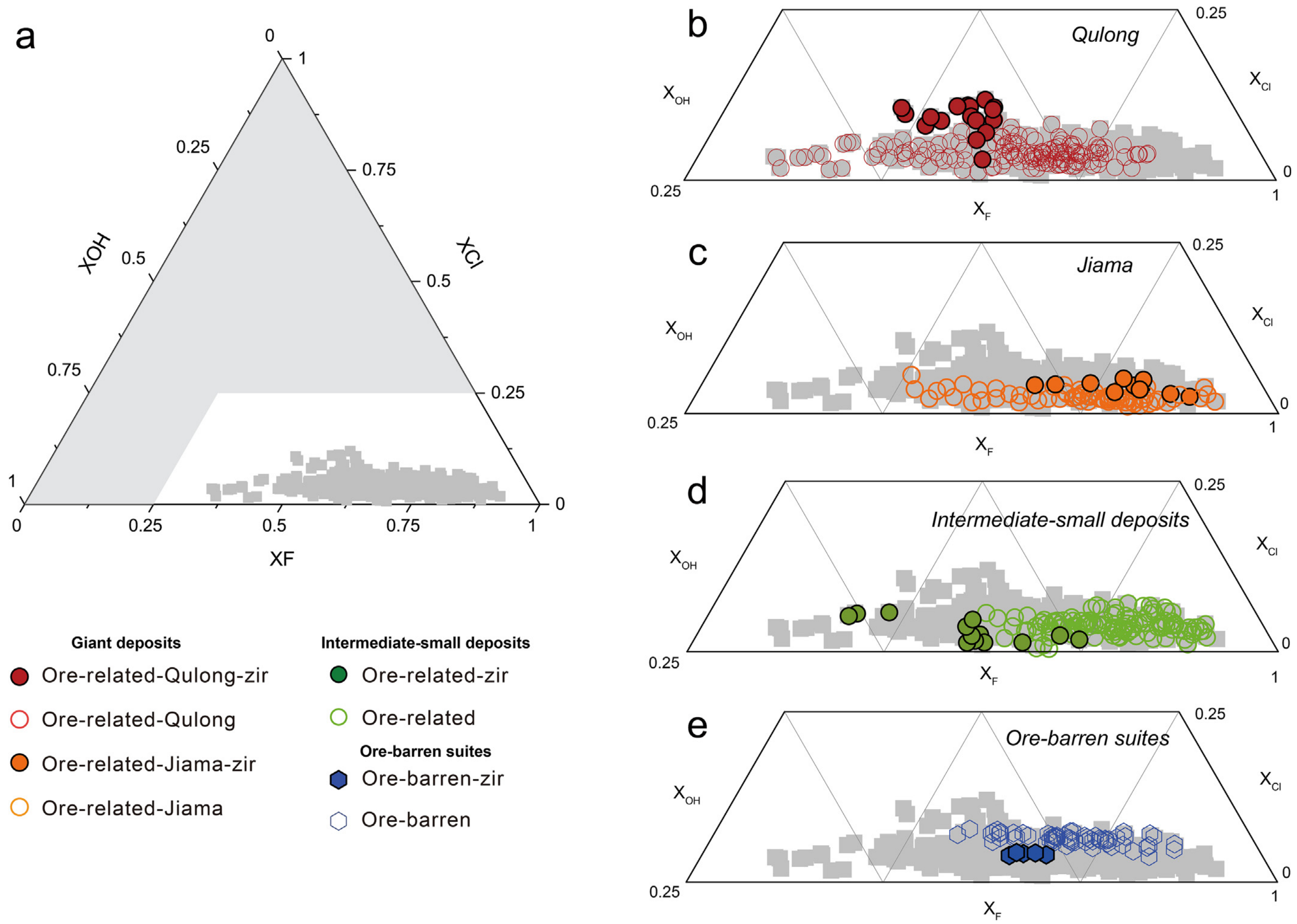


**Fig. 3.** Ternary diagrams showing apatite volatile compositions of collected samples. Solid circles represent apatite inclusions in zircon that are from this study and hollow circles represent apatite in matrix that are collected from other studies. Majority of apatite data are distributed along $X_F$-$X_{OH}$ line and mostly enriched in $X_F$ (a). The diagrams in the right panel are apatite data in separate systems from (b) Qulong giant deposit, (c) Jiama giant deposit, (d) intermediate-small deposits and (e) ore-barren suites.

identify alternative sets of initial parameters that similarly match the modelled trend (Supplementary Data Fig. 1-4; Humphreys et al., 2021; Lormand et al., 2024). More details to the description of the model are displayed in Methods and in Humphreys et al. (2021) and Lormand et al. (2024). The advantage of such forward modeling is that it uses all relevant apatite data to find the best-fit magmatic condition, which avoids the ambiguity in interpreting single apatite volatile data points.

Since the apatite of similar affinity (Qulong, Jiama, other deposits, or barren) can be from diverse magma systems at diverse stages of evolution, nearly all parameters used for the modeled magmatic conditions come with a range to reproduce the natural situation (Tables 1 and 2). Through modeling the apatite data in $X_F/X_{OH}$ vs. $X_{Cl}/X_{OH}$ and $X_F/X_{Cl}$ vs. $X_{Cl}/X_{OH}$ spaces (Figs. 5 and 6), the volatile evolution path of magma is visualized: before the magma reaches water saturation, variation in magma volatile contents is dominantly controlled by fractional crystallization and described by bulk crystal-melt partition coefficient ($D^{c/m}_{volatile}$). The $D^{c/m}_{volatile}$ of F, Cl and $H_2O$ is correlated with the incompatibility of each element, and the incompatibilities of F, Cl and $H_2O$ follow the order of Cl > OH > F (Chambefort et al., 2013; Van den Bleeken and Koga, 2015; Li and Hermann, 2017).

Therefore, as a hydrous, $H_2O$-undersaturated magma evolves, $X_{Cl}/X_{OH}$ in apatite increases, $X_F/X_{Cl}$ and $X_F$/OH decrease. In this model, as the magma reaches water saturation, the partition coefficients between fluid and melt ($D^{f/m}_{volatile}$) also start to affect volatile concentrations. Since there is major difference between fluorine and chlorine in $D^{f/m}_{volatile}$ ($D^{f/m}_{Cl}$ = 8–25; $D^{f/m}_{F}$ = 0.5–1.5; Signorelli and Carroll, 2000; Balcone-Boissard et al., 2009; Iveson et al., 2017), chlorine is strongly extracted by exsolved fluid phase, while only a small amount of fluorine fractionates into the fluid. This drives a sharp decrease in $X_{Cl}/X_{OH}$ and slight decrease of $X_F/X_{OH}$ of apatite. Similarly, the $X_F/X_{Cl}$ ratio starts to increase after fluid saturation (Figs. 5 and 6). Notably, the evolution paths of all systems show similar general trend, which suggests that the magmas are hydrous and initially $H_2O$-undersaturated (Figs. 5 and 6), the differences lie in values of parameters used in modeling each system (Table 1).

## 7. Discussion

### 7.1. 'Target curve' and possible range of magmatic volatile compositions

We use forward MATLAB program modeling from Humphreys et al. (2021) and Lormand et al. (2024) to reconstruct the magmatic volatiles evolution of porphyry deposit magma system. As discussed in the modeling result, we build the 'target curve' to fit natural apatite inclusions in zircon (Figs. 5 and 6) and explore possible volatile composition. The parameter used for 'target curve' are listed in Table 1. As discussed above, before and after magma reach water saturation, apatite $X_{Cl}/X_{OH}$ and $X_F/X_{OH}$ display different trends (Stock et al., 2018; Humphreys et al., 2021; Popa et al.,

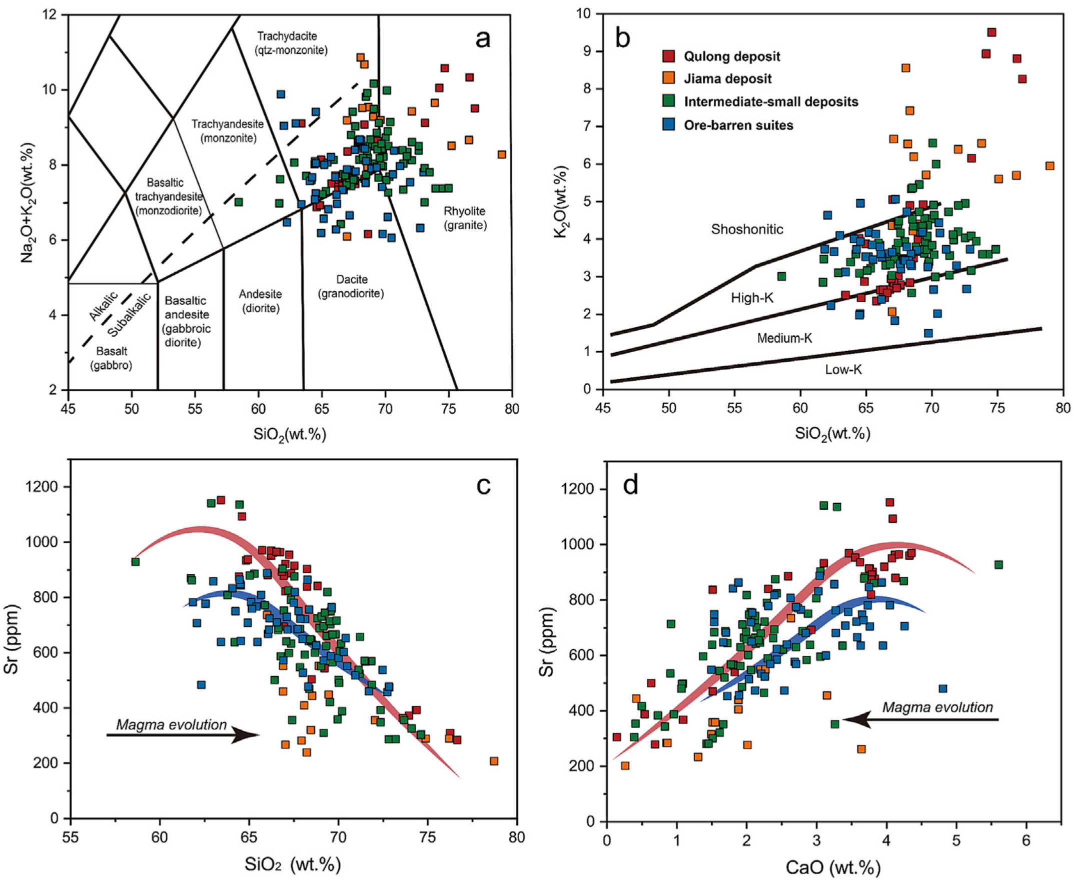


**Fig. 4.** Major element diagrams of compiled whole rock data. The red and blue stripes are fitted curves of ore-related and ore-barren dataset. (a) ($Na_2O + K_2O$) vs. $SiO_2$ (after Irvine and Baragar, 1971; Middlemost, 1994); (b) $K_2O$ vs. $SiO_2$ (after Peccerillo and Taylor, 1976; Rollinson, 2014); (c) Sr vs. $SiO_2$; (d) Sr vs. CaO. (For interpretation of the references to color in this figure legend, the reader is referred to the web version of this article.)

**Table 2**
Range of volatile contents and water saturation level.

| Type | Initial melt volatile concentrations | | | $H_2O$ saturation level |
|---|---|---|---|---|
| | $H_2O$ (wt.%) | Cl (wt.%) | F (wt.%) | $H_2O$ (wt.%) |
| Qulong | 5.5–8.5 | 0.06–0.12 | 0.03–0.13 | ~9.5–11.5 |
| Jiama | 5.5–7.1 | 0.05–0.15 | 0.12–0.15 | ~9–11 |
| Intermediate-small deposits | 5.5–6.7 | 0.05–0.15 | 0.12–0.15 | ~6–8 |
| Ore-barren suites | 4.3–4.7 | 0.09–0.12 | 0.08–0.12 | ~5–7 |

2021). Therefore, we can use $X_{Halogen}/X_{OH}$ as an indicator of the stage of volatile evolution. We can tell that porphyry deposit magma system was initially water-undersaturated and became water-saturated during fractionation (Figs. 5 and 6). However, we must point out that although the numerical simulation considers the complexity of magmatic processes, the collected apatite data can rarely reflect the volatile unsaturated stage of porphyry deposit magma system, so our constrain on volatile unsaturated stage maybe not so robust. Considering the statistical errors, we use multi-start regression analysis to help exploring possible range of magma volatile composition. And our research mainly focuses on the saturated water content of different ore-related/ore-barren magma system.

### *7.2. Different magmatic water conditions between ore-related and ore-barren magmas*

Previous studies have demonstrated that ore-forming magmas are hydrous ($H_2O$ > 4 wt.%). Accumulated magmatic water changes the crystallization sequence of igneous minerals and leads to early and prolific production of amphibole and causes the early increase of Sr content. We have systematically compiled 167 sets of whole rock geochemical data for this study (Fig. 4), covering Miocene ore-related and ore-barren magmatic rocks from the Gangdese belt. The early stage increases of Sr contents (Fig. 4c,d) indicated the lack of notable plagioclase crystalization and early formation of amphibole which means qualitatively that both ore-related and ore-barren magma are hydrous (Richards, 2011a; Wang et al., 2014a; Yang et al., 2015), we can hardly tell their volatile differences using whole rock data. Then a question arose: how to quantitatively tell the differences between ore-barren and ore-related magma. To solve this question, we use apatite and numerical model to compare their hydrous features.

As Figs. 5 and 6 show, we have quantitatively modelled the observed apatite volatile trends of giant deposit (Qulong and Jiama deposit), intermediate-small deposits and ore-barren suites from Gangdese belt. For each unit, we visually defined a target curve to reproduce the compositions of the zircon-hosted apatite inclusions. This target curve is generated by adjusting pre-defined initial volatile contents ($H_2O$, Cl, and F), bulk crystal-melt partition coef-

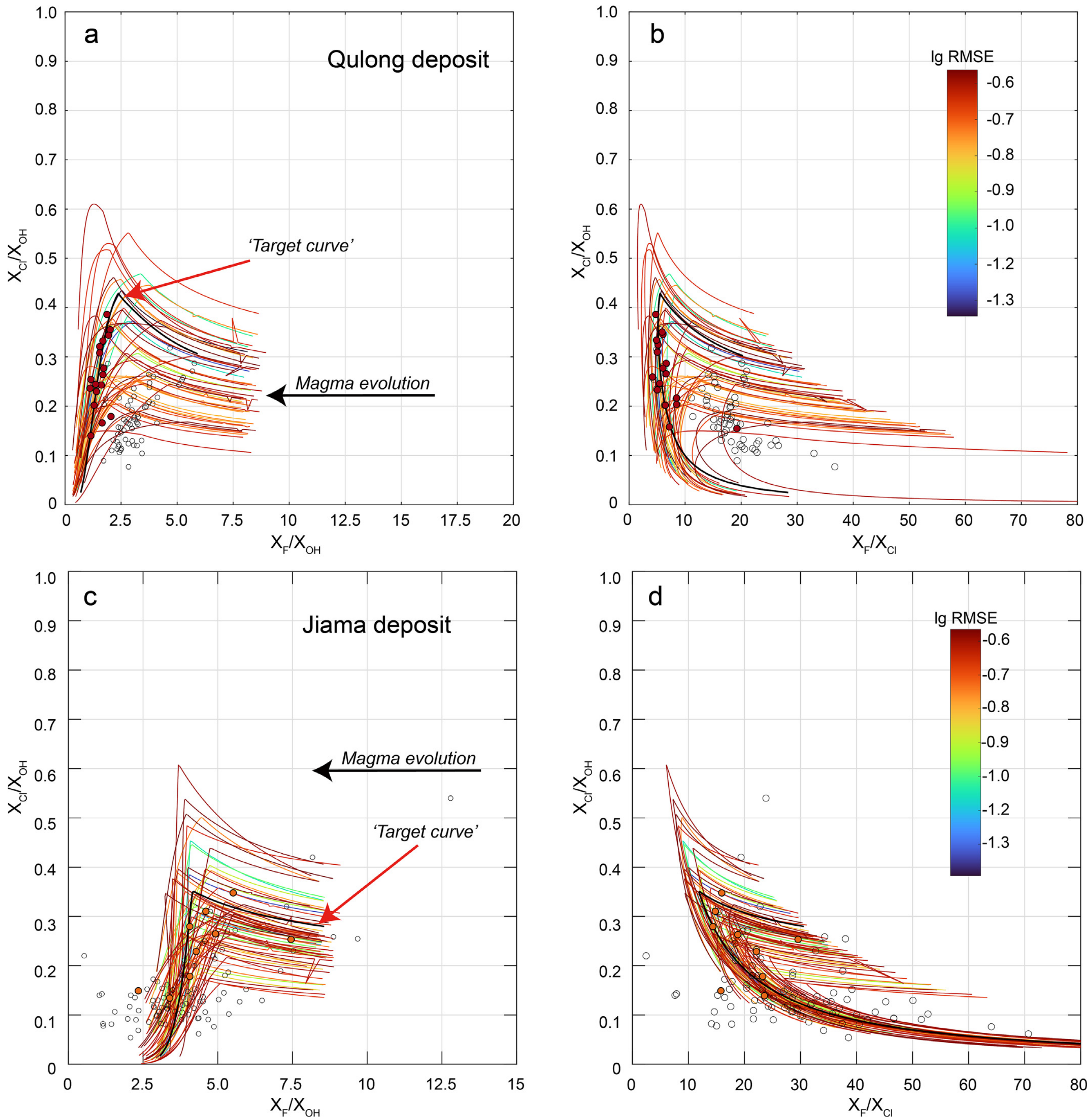


**Fig. 5.** Modeling of giant porphyry copper deposits (Qulong, a and b; Jiama, c and d). Apatite volatile compositions (small black circles) plotted as $X_{Cl}/X_{OH}$ vs $X_F/X_{OH}$ (left) and $X_{Cl}/X_{OH}$ vs $X_F/X_{Cl}$ (right) and the target curve (black) and alternative successful runs (colored lines). The inset bar shows the scale of root mean square error (log(RMSE)) of modelled lines relative to the target curve. The target curve is defined using the zircon-hosted apatite inclusions, and multistart result are defined for the whole dataset. The solid color circles are our apatite inclusion data, the hollow circles are compiled matrix apatite data.

ficients ($D^{xl\text{-}m}$), and apatite-melt-fluid partition coefficient ($D^{fl\text{-}m}$) on the basis of previous experimental petrology work (Ionov et al., 1997; Li and Hermann, 2017; Stock et al., 2018; Li and Costa, 2020).

Using the results of numerical modelling of the natural apatite dataset, we constrain the water contents of ore-related and ore-barren magma. Interestingly, the starting magmatic water contents among these systems are different (Table 2). Ore-barren magmatic systems have lowest initial water of 4.3–4.7 wt.%, lower than those of ore-related magma (5.5–7.2 wt.%, Table 2). This is indeed within the range of water contents of basaltic arc magma (2–6 wt.%; Zimmer et al., 2010; Plank et al., 2013). Despite "lowest" water content, the ore-barren magma is still hydrous with its water content > 4 wt.%. However, their water saturation level varies differently, 7–10 wt.% for ore-related magma and 6 wt.% for ore-barren magma. The source of such high initial water content can be worth discussing: primary arc magma is hydrous owing to the contribution from dehydration of subducting oceanic plate and sediments (Richards, 2011a), while studied rocks here occurred in post-subduction period (Miocene) in the absence of a subduct-

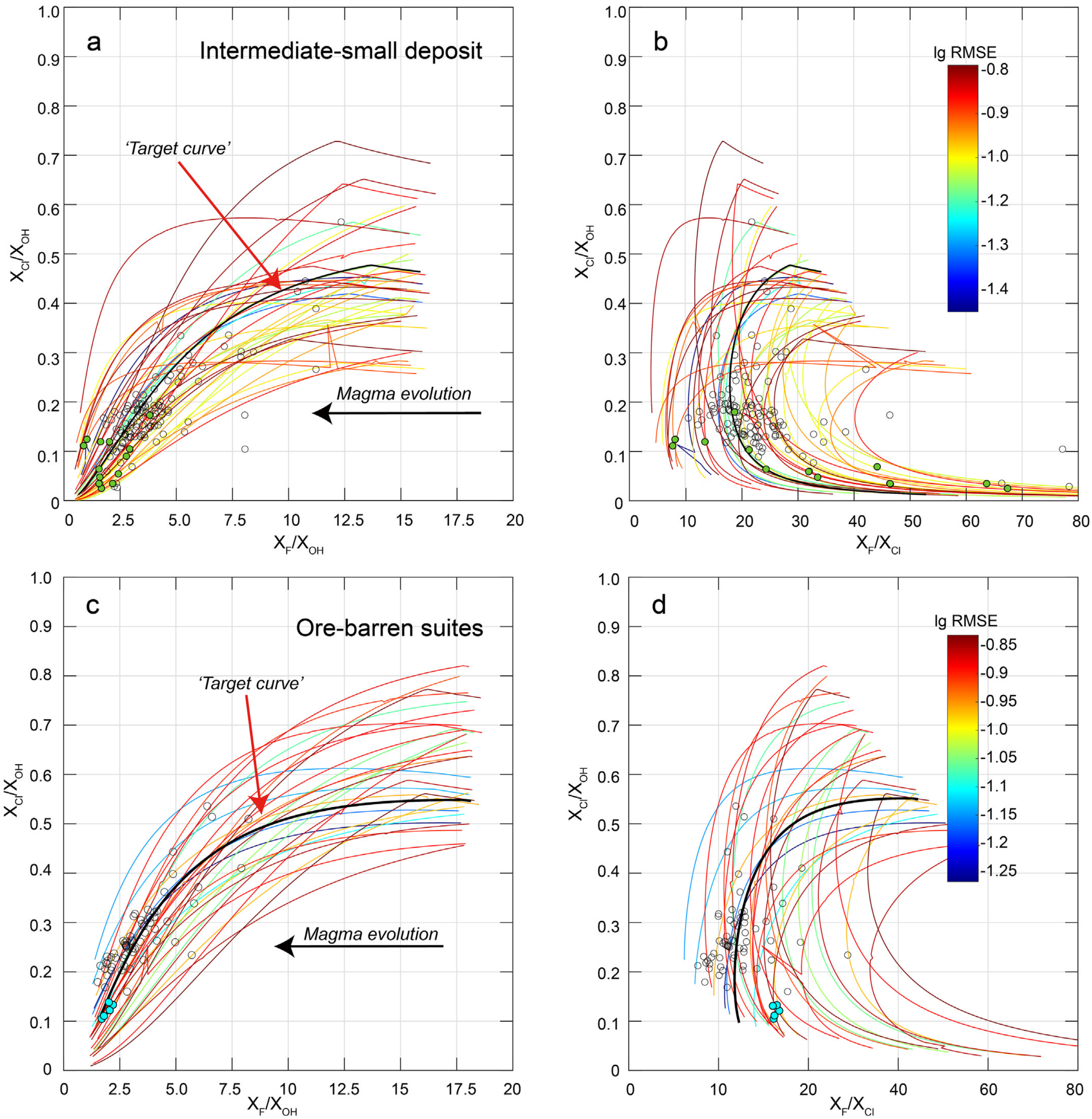


**Fig. 6.** Modeling results of intermediate-small porphyry deposits (a, b) and ore-barren suites (c, d). The solid color circles are our apatite inclusion data, the hollow circles are compiled apatite phenocryst data.

ing oceanic slab. In post-subduction setting, the injection and assimilation of mantle-derived hydrous ultrapotassic melt are proposed to be a main additional source of water (e.g., Yang et al., 2015, 2016; Wang et al., 2018, 2022; Shen et al., 2021). Another potential water source is through the dehydration reactions of continental subducted plate (e.g., Zheng et al., 2013). The modeled results show that the Miocene granitoids are similarly hydrous when initially generated. In addition to modeling, similarly high initial contents of Sr between the ore-related and barren systems are also compatible with their similarity in initial water contents (Fig. 4).

Initial magmatic water contents influence the fertility of ore-forming magma according to our model. Previous studies have suggested that the ore-forming high-Sr/Y adakitic rocks in Gangdese belt are linked to water-fluxed partial melting of hydrated lower crust (Hou et al., 2004; Wang et al., 2014b; Lu et al., 2015; Hou and Wang, 2019; Xu et al., 2023). The Gangdese Miocene granitoids show hybrid isotopic compositions generated by mixing of adakitic melt and mantle-derived ultrapotassic melts (Yang et al., 2015; Wang et al., 2018). The ascent of ultrapotassic magma into the lower crust was accompanied by high degrees of anhydrous mineral fractionation (Wang et al., 2018), such as olivine, and therefore the magmas were able to release water to stimulate lower crustal water-fluxed melting. Higher degree of lower crust partial melting can further promote fractionation of essential nutrients such as Cu, S into the magma (Hou et al., 2015a, b). However, even if these adakitic magmas are initially hydrous, only some of these systems can ultimately result in the economic endowment of Cu. Although some adakitic rocks in the Gangdese belt are associated with mineralized systems (e.g., Qulong, Jiama), the rest of them ends up with unmineralized systems (e.g., Linzhi, Mayum), suggesting the initial water enrichment of magma system is not the critical factor to the final metal endowments. Before primary magma emplaces in the shallow crustal reservoir and contributes to the mineralization of Cu, it may undergo multiple stages of fractionation, assimilation, and mixing (Richards, 2022), all these processes can make differences to magmatic water contents.

### 7.3. Porphyry Cu mineralization controlled by magma storage pressure

Although both ore-related and ore-barren magma systems are hydrous, they show largest variations in the threshold of water saturation contents. Barren systems have a saturation level of 6 wt.%, 7 wt.% for mineralized systems, and as high as 10 wt.% for giant deposits of Qulong and Jiama, which is similar with the estimation of Lu et al. (2015). The case of giant deposits can be noteworthy: according to estimation, a saturation level of 10 wt.% $H_2O$ for albitic melt is related to 0.4 GPa, 12 km intrusion depth, while ~0.4 GPa and ~14 km for basaltic magma owing to different melt composition (Behrens et al., 2009; Plank et al., 2013; Chiaradia, 2020; Fig. 7). The ore-forming magma is normally highly evolved (e.g., granitic, dacitic) in shallow reservoir, but it seems that a depth of 14 km is still overly deep for 5 km depth at which porphyry mineralization event is supposed to occur (Yang et al., 2009; Sillitoe, 2010; Huang et al., 2023b). Indeed, as suggested by a number of studies (e.g., Yang et al., 2015; Richards, 2018, 2022), an underlying giant, water-rich magma chamber exists (5–15 km) below the shallow ore-forming intrusions (3–5 km) (Fig. 7). This indicates that the deep magma reservoir has already started exsolving gas, but in the style of closed system exsolution without losing volatiles. Such deep stored magma may massively exsolve fluids once being elevated to a shallower level, either through branching an apophysis, or through tectonic uplifting.

Goltz et al. (2020) estimated the water content of primitive melts crystallizing amphibole using amphibole inclusions in high forsterite olivine and proposed that the primitive melt was super hydrous (i.e., >8 wt.% $H_2O$). They found that the hydrous primitive melt had water contents of 10–14 wt.% $H_2O$ at depths of 23.6–28.8 km. According to our model, magmas from giant deposits generally have relatively enriched initial water contents of 5.5–7.2 wt.% and can reach saturation simply through fractionation. Previous studies have demonstrated the injection and assimilation of hydrous ultrapotassic magma from deep reservoir beneath the shallow mineralized system provide additional volatile and water contents (e.g., Yang et al., 2015; Wang et al., 2018). During Neo-Tethyan oceanic plate subduction, the lower crust has undergone metasomatization by arc magmatism, becoming enriched in volatiles, such as water. A series of arc-magma-like geochemical characteristics of local adakitic rocks whether mineralized or not, such as high LILE, low HFSE, and mantle-like Sr-Nd-Hf isotope compositions, indicate the contribution of arc magmatism in their lower crust source (Wang et al., 2021, 2022). Indeed, adakitic rocks have been considered to be related to a hydrous magmatic system, in which fractionation of Sr-rich plagioclase is suppressed and Y-rich amphibole is promoted to make the high Sr/Y ratio of adakitic rocks (e.g., Zimmer et al., 2010). In addition to the pre-enriched lower crust hypothesis, some research also suggested injection of ultrapotassic magma can be responsible in the primarily hydrous condition of these magmas, due to its remarkable capability of accommodating water (Yang et al., 2015, 2016).

For barren systems and less mineralized systems, even though their initial water contents (4.3–4.7 wt.% for barren ones and 5.5–7.2 wt.% for mineralized ones) can still be remarkable compared to other igneous rocks without adakitic affinities (e.g., Richards, 2011a; Wang et al., 2014a), lower water saturation level indicates these magma systems do not reach a water content (4.4 wt.% and 5.6 wt.%) as enriched as that of giant deposits (10 wt.%) before saturated. This can be attributed to higher extent of assimilation with dry crust, mixing with damp magma, or shallower emplacement cause dilution of magmatic water. In addition, emplacement of these magma systems at shallow levels will less likely lead to massive fluid exsolution, because of the limited amount of fluid available to be released.

### 7.4. Implication to porphyry metallogenesis process: Dramatic uplifting is the key

A key discovery of this study is that large-scale porphyry mineralization systems are associated with deeper water saturation level, while there are some systematic differences of initial magmatic water contents [$H_2O_{(i)}$] and bulk crystal-melt partition coefficient of water [$D^{c/m}_{H2O}$] exists among barren systems, moderately mineralized and strongly mineralized systems (Tables 1-3, Figs. 5–6). However, economic enrichment of metals must occur at an explorable shallow depth. The question therefore lies in how increased storage depth can be related to larger scale porphyry mineralization.

The role of a contractional setting in porphyry metallogenesis is widely recognized as important. A crustal thickening or compress environment is advantageous for the formation of a large magma reservoir and prolong magma activity with hydrous evolving magma, which is critical for the porphyry ore-forming process (Sillitoe, 2010; Richards, 2011b; Park et al., 2021; Wu et al., 2023). In convergent settings, the constant thickening of the crust can promote rapid exhumation and surface uplifting. This process leads to the unloading of lithostatic pressure around the large ore-forming magma chamber. The uplifting of the chamber is indeed a vital factor in the mineralization processes observed in a series of porphyry systems along the Cordillera (Hill et al., 2002; Cooke et al., 2005).

In the Gangdese porphyry metallogenic belt, southern Tibet, a period of intensified exhumation is believed to have taken place from 25–10 Ma (Dai et al., 2013; Cao et al., 2020; Shen et al., 2020; Li et al., 2022), corresponding well to the focused porphyry mineralization event at ~16–14 Ma (Wang et al., 2018; Yang and Cooke, 2019). Although the mechanism causing such accelerated exhumation remains disputed (the majority believes that crustal shortening related to the Gangdese thrust system is the key), such an exhumation event can have played a critical role in the mineralization event. Based on estimation by Cao et al. (2020), this rapid exhumation event has likely uplifted the crust by 5–6 km. If we consider the estimated intrusion depth of 14 km for granitic magma, which correlates with a water saturation level of 10 wt.%, the uplift could bring the magma chamber to a depth suitable for metallogenesis, around 8 km. Additionally, Li et al. (2022) proposed the existence of an extra-high elevation in southern Tibet at 17.3 Ma, caused by rapid surface uplift by ca. 20 Ma followed initial slab break-off.

We hypothesize that the ore-related magma chamber did not undergo extensive crystallization but rapidly ascended to a shallow level. This rapid ascent led to a drastic drop in pressure, causing massive fluid exsolution within a short time period (Richards, 2018). In contrast, the barren granites, which did not produce giant porphyry Cu deposits, may be attributed to two factors. Firstly, the

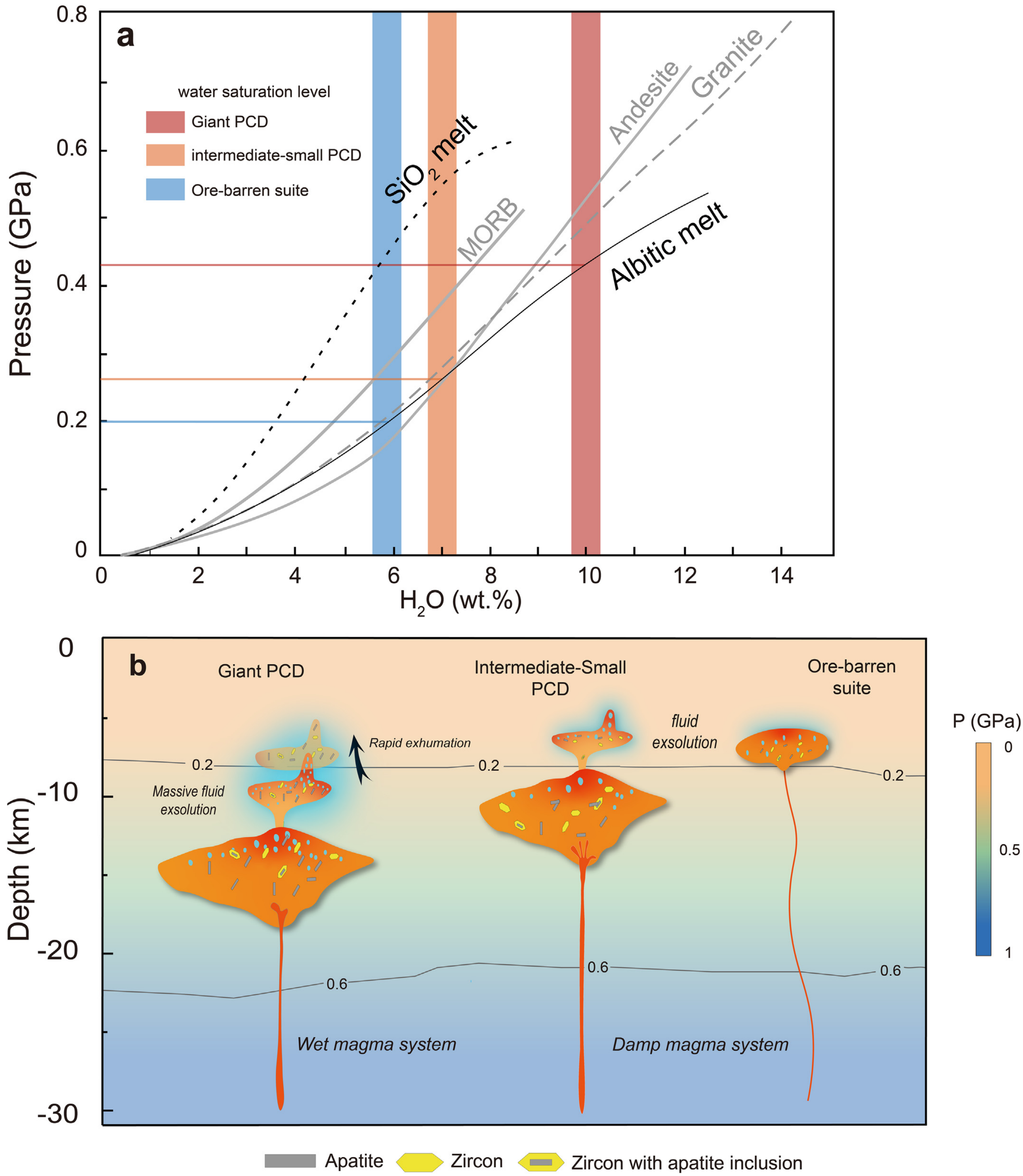


**Fig. 7.** (a) Solubility of water as a function of pressure and magma composition. Generally, the water solubility is positively correlated to pressure and silica contents (Behrens et al., 2009; Baker and Alletti, 2012). Colored columns correspond to the modeled water saturation levels of three systems (10 wt.% for giant, 7 wt.% for intermediate-small, and 6 wt.% for barren) and their corresponding pressure. (b) Conceptual cartoon illustrating the correlation between magmatic water evolution and PCD mineralization in the case of the Gangdese belt. Primary magmas can be moderately hydrous whether for mineralized or barren systems (likely because of remelting of pre-enriched lower crust or injection of ultrapotassic magma), but the giant PCDs can reach water saturation and pool at deeper levels (~14 km), while magmas of smaller PCD or barren system saturate at shallow level. Shallow and slow saturation without prolific fluid results in low impact fluid exsolution, however, deeper stored hydrous magma reservoir can be dramatically emplaced due to tectonic uplifting and exhumation which causing massive fluid exsolution favored by large-scaled mineralization. The scale of crustal pressure gradient is provided by Philpotts and Ague (2009) and Sheng et al. (2020).

**Table 3**
Range of volatile partition coefficients between crystal/fluid and melt.

| Type | $D_{crys-melt}$ | | $D_{fluid-melt}$ | |
|---|---|---|---|---|
| | Cl | F | Cl | F |
| Qulong | 0.14–0.16 | 1.8–2.2 | 10–18 | 1.3–1.5 |
| Jiama | 0.24–0.26 | 1.4–1.7 | 10–20 | 0.8–1.6 |
| Intermediate-Small deposits | 0.24–0.26 | 1.4–1.7 | 10–20 | 0.5–1.6 |
| Ore-barren suites | 0.31–0.33 | 1.8–2.0 | 8–25 | 1.5–2.5 |

barren magmas may have been too water-poor to reach fluid saturation. Alternatively, the barren intrusions may have been uplifted to an inappropriate depth, hindering and delaying the explosive degassing process. As a result, the metals would disperse instead of being focused into mineralized apophyses.

## 8. Conclusion

In this study, we used apatite zircon inclusions and forward Geo-modeling techniques to effectively constrain the thresholds for magmatic initial and saturated water content. Our research findings strongly indicate that both ore-related and ore-barren magma systems exhibit a significant degree of hydration. Additionally, the modeled magmatic water contents display considerable variations across ore-related and ore-barren magma systems. Combined with previous studies, we proposed that the primary discrepancy lies in the initial and saturation threshold of water, with a value of 6.0 wt.% for ore-barren systems and up to 10.0 wt.% for highly mineralized systems.

In light of the comprehensive analysis conducted, which includes the whole rock geochemistry data, apatite volatile composition, and modeling techniques, we proposed that the ore-related magma is stored at greater depths, thereby exhibiting higher water solubility. As a result, we propose that the level of magmatic water saturation plays a pivotal role in the formation of porphyry copper systems. It is noteworthy that magma with mineralization potential not only demonstrates elevated water solubility but also experiences substantial water enrichment upon reaching saturation. Moreover, the deeper storage depth and injection of hydrous mafic magma are likely contributing factors to the augmented water solubility observed. What's more, the significance of ultrapotassic magma in the genesis of porphyry copper deposits necessitates further investigation.

## CRediT authorship contribution statement

**Yingcai Sun:** Writing – review & editing, Writing – original draft, Visualization, Software, Methodology, Data curation, Conceptualization. **Qiushi Zhou:** Writing – review & editing, Writing – original draft, Methodology, Investigation, Conceptualization. **Rui Wang:** Writing – review & editing, Validation, Supervision, Methodology, Conceptualization. **Madeleine C.S. Humphreys:** Writing – review & editing, Validation, Software, Methodology.

## Declaration of competing interest

The authors declare that they have no known competing financial interests or personal relationships that could have appeared to influence the work reported in this paper.

## Acknowledgement

This study is financially supported by the National Key R&D Program of China (2022YFF0800902), National Natural Science Foundation of China (42225204, 42121002), Fundamental Research Funds for the Central Universities (grant numbers 2652023001; 2-9-2023-202), and the 111 project (B18048). M.C. S.H. was supported by funding from the European Research Council (ERC) under the European Union's Horizon 2020 research and innovation program (grant agreement No. 864923).

## Appendix A. Supplementary data

Supplementary data to this article can be found online at https://doi.org/10.1016/j.gsf.2024.101962.

## References

Baker, D.R., Alletti, M., 2012. Fluid saturation and volatile partitioning between melts and hydrous fluids in crustal magmatic systems: the contribution of experimental measurements and solubility models. Earth-Sci. Rev. 114, 298–324. https://doi.org/10.1016/j.earscirev.2012.06.005.

Balcone-Boissard, H., Michel, A., Villemant, B., 2009. Simultaneous determination of fluorine, chlorine, bromine and iodine in six geochemical reference materials using pyrohydrolysis, ion chromatography and inductively coupled plasma-mass spectrometry. Geostand. Geoanal. Res. 33, 477–485. https://doi.org/10.1111/j.1751-908X.2009.00018.x.

Behrens, H., Misiti, V., Freda, C., Vetere, F., 2009. Solubility of $H_2O$ and $CO_2$ in ultrapotassic melts at 1200 and 1250 °C and pressure from 50 to 500 MPa. Am. Mineral. 94, 105–120. https://doi.org/10.2138/am.2009.2796.

Bell, E.A., Boehnke, P., Hopkins-Wielicki, M.D., Harrison, T.M., 2015. Distinguishing primary and secondary inclusion assemblages in Jack Hills zircons. Lithos 234–235, 15–26. https://doi.org/10.1016/j.lithos.2015.07.014.

Brenan, J., 1993. Kinetics of fluorine, chlorine and hydroxyl exchange in fluorapatite. Chem. Geol. 110, 195–210.

Cao, W., Yang, J., Zuza, A.V., Ji, W.-Q., Ma, X.-X., Chu, X., Burgess, Q.P., 2020. Crustal tilting and differential exhumation of Gangdese Batholith in southern Tibet revealed by bedrock pressures. Earth Planet. Sci. Lett. 543, 116347. https://doi.org/10.1016/j.epsl.2020.116347.

Chambefort, I., Dilles, J.H., Longo, A.A., 2013. Amphibole geochemistry of the Yanacocha volcanics, Peru: evidence for diverse sources of magmatic volatiles related to gold ores. J. Petrol. 54, 1017–1046. https://doi.org/10.1093/petrology/egt004.

Chiaradia, M., 2020. How much water in basaltic melts parental to porphyry copper deposits? Front. Earth Sci. 8, 138. https://doi.org/10.3389/feart.2020.00138.

Chiaradia, M., Caricchi, L., 2017. Stochastic modelling of deep magmatic controls on porphyry copper deposit endowment. Sci. Rep. 7, 44523. https://doi.org/10.1038/srep44523.

Cooke, D.R., Hollings, P., Walshe, J.L., 2005. Giant porphyry deposits: characteristics, distribution, and tectonic controls. Econ. Geol. 100, 801–818.

Dai, J., Wang, C., Hourigan, J., Li, Z., Zhuang, G., 2013. Exhumation history of the Gangdese batholith, Southern Tibetan Plateau: evidence from apatite and zircon (U-Th)/He thermochronology. J. Geol. 121, 155–172. https://doi.org/10.1086/669250.

Goldoff, B., Webster, J.D., Harlov, D.E., 2012. Characterization of fluor-chlorapatites by electron probe microanalysis with a focus on time-dependent intensity variation of halogens. Am. Mineral. 97, 1103–1115. https://doi.org/10.2138/am.2012.3812.

Goltz, A.E., Krawczynski, M.J., Gavrilenko, M., Gorbach, N.V., Ruprecht, P., 2020. Evidence for superhydrous primitive arc magmas from mafic enclaves at Shiveluch volcano, Kamchatka. Contrib. Mineral. Petrol. 175, 115. https://doi.org/10.1007/s00410-020-01746-5.

Hill, K.C., Kendrick, R.D., Crowhurst, P.V., Gow, P.A., 2002. Copper-gold mineralisation in New Guinea: tectonics, lineaments, thermochronology and structure. Aust. J. Earth Sci. 49, 737–752. https://doi.org/10.1046/j.1440-0952.2002.00944.x.

Hou, Z., Duan, L., Lu, Y., Zheng, Y., Zhu, D., Yang, Z., Yang, Z., Wang, B., Pei, Y., Zhao, Z., McCuaig, T.C., 2015a. Lithospheric architecture of the Lhasa Terrane and its control on ore deposits in the Himalayan-Tibetan Orogen. Econ. Geol. 110, 1541–1575. https://doi.org/10.2113/econgeo.110.6.1541.

Hou, Z., Gao, Y., Qu, X., Rui, Z., Mo, X., 2004. Origin of adakitic intrusives generated during mid-Miocene east–west extension in southern Tibet. Earth Planet. Sci. Lett. 220, 139–155. https://doi.org/10.1016/S0012-821X(04)00007-X.

Hou, Z., Wang, R., 2019. Fingerprinting metal transfer from mantle. Nat. Commun. 10, 3510. https://doi.org/10.1038/s41467-019-11445-w.

Hou, Z., Yang, Z., Lu, Y., Kemp, A., Zheng, Y., Li, Q., Tang, J., Yang, Z., Duan, L., 2015b. A genetic linkage between subduction- and collision-related porphyry Cu deposits in continental collision zones. Geology 43, 247–250. https://doi.org/10.1130/G36362.1.

Huang, W., Stock, M.J., Xia, X.-P., Sun, X., Cui, Z., Liuyun, O., Zhang, J., Chen, X., Zheng, Y., Liang, H., 2023a. Determining the impact of magma water contents on porphyry Cu fertility: constraints from hydrous and nominally anhydrous mineral analyses. GSA Bull. 136, 673–688. https://doi.org/10.1130/B36871.1.

Huang, M.L., Zhu, J.J., Chiaradia, M., Hu, R.Z., Xu, L.L., Bi, X.-W., 2023b. Apatite volatile contents of porphyry Cu deposits controlled by depth-related fluid exsolution processes. Econ. Geol. 118, 1201–1217. https://doi.org/10.5382/econgeo.5000.

Humphreys, M.C.S., Smith, V.C., Coumans, J.P., Riker, J.M., Stock, M.J., de Hoog, J.C.M., Brooker, R.A., 2021. Rapid pre-eruptive mush reorganisation and atmospheric volatile emissions from the 12.9 ka Laacher See eruption, determined using apatite. Earth Planet. Sci. Lett. 576, 117198. https://doi.org/10.1016/j.epsl.2021.117198.

Ionov, D.A., Griffin, W.L., O'Reilly, S.Y., 1997. Volatile-bearing minerals and lithophile trace elements in the upper mantle. Chem. Geol. 141, 153–184. https://doi.org/10.1016/S0009-2541(97)00061-2.

Irvine, T.N., Baragar, W.R.A., 1971. A guide to the chemical classification of the common volcanic rocks. Can. J. Earth Sci. 8, 523–548. https://doi.org/10.1139/e71-055.

Iveson, A.A., Webster, J.D., Rowe, M.C., Neill, O.K., 2017. Major element and halogen (F, Cl) mineral–melt–fluid partitioning in hydrous rhyodacitic melts at shallow crustal conditions. J. Petrol. 58, 2465–2492. https://doi.org/10.1093/petrology/egy011.

Ji, W.-Q., Wu, F.-Y., Chung, S.-L., Li, J.-X., Liu, C.-Z., 2009. Zircon U–Pb geochronology and Hf isotopic constraints on petrogenesis of the Gangdese batholith, southern Tibet. Chem. Geol. 262, 229–245. https://doi.org/10.1016/j.chemgeo.2009.01.020.

Kendall-Langley, L.A., Kemp, A.I.S., Hawkesworth, C.J., EIMF, Craven, J., Talavera, C., Hinton, R., Roberts, M.P., 2021. Quantifying F and Cl concentrations in granitic melts from apatite inclusions in zircon. Contrib. Mineral. Petrol. 176, 58. https://doi.org/10.1007/s00410-021-01813-5.

Li, Y., Allen, M.B., Li, X.-H., 2022. Millennial pulses of ore formation and an extra-high Tibetan Plateau. Geology 50, 665–669. https://doi.org/10.1130/G49911.1.

Li, W., Costa, F., 2020. A thermodynamic model for F-Cl-OH partitioning between silicate melts and apatite including non-ideal mixing with application to constraining melt volatile budgets. Geochim. Cosmochim. Acta 269, 203–222. https://doi.org/10.1016/j.gca.2019.10.035.

Li, H., Hermann, J., 2017. Chlorine and fluorine partitioning between apatite and sediment melt at 2.5 GPa, 800 °C: a new experimentally derived thermodynamic model. Am. Mineral. 102, 580–594. https://doi.org/10.2138/am-2017-5891.

Lormand, C., Humphreys, M.C.S., Colby, D.J., Coumans, J.P., Chelle-Michou, C., Li, W., 2024. Volatile budgets and evolution in porphyry-related magma systems, determined using apatite. Lithos 480–481, 107623. https://doi.org/10.1016/j.lithos.2024.107623.

Loucks, R.R., 2014. Distinctive composition of copper-ore-forming arc magmas. Aust. J. Earth Sci. 61, 5–16. https://doi.org/10.1080/08120099.2013.865676.

Lu, Y.-J., Loucks, R.R., Fiorentini, M.L., Yang, Z.-M., Hou, Z.-Q., 2015. Fluid flux melting generated postcollisional high Sr/Y copper ore–forming water-rich magmas in Tibet. Geology 43, 583–586. https://doi.org/10.1130/G36734.1.

Middlemost, E.A.K., 1994. Naming materials in the magma/igneous rock system. Earth-Sci. Rev. 37, 215–224. https://doi.org/10.1016/0012-8252(94)90029-9.

Müntener, O., Kelemen, P.B., Grove, T.L., 2001. The role of $H_2O$ during crystallization of primitive arc magmas under uppermost mantle conditions and genesis of igneous pyroxenites: an experimental study. Contrib. Mineral. Petrol. 141, 643–658. https://doi.org/10.1007/s004100100266.

Park, J.-W., Campbell, I.H., Chiaradia, M., Hao, H., Lee, C.-T., 2021. Crustal magmatic controls on the formation of porphyry copper deposits. Nat. Rev. Earth Environ. 2, 542–557. https://doi.org/10.1038/s43017-021-00182-8.

Peccerillo, A., Taylor, S.R., 1976. Geochemistry of Eocene calc-alkaline volcanic rocks from the Kastamonu area, Northern Turkey. Contrib. Mineral. Petrol. 58, 63–81. https://doi.org/10.1007/BF00384745.

Philpotts, A.R., Ague, J.J., 2009. Principles of Igneous and Metamorphic Petrology. Cambridge University Press, Cambridge, UK, p. 667.

Piccoli, P.M., Candela, P.A., 2002. Apatite in igneous systems. Rev. Mineral. Geochem. 48, 255–292. https://doi.org/10.2138/rmg.2002.48.6.

Plank, T., Kelley, K.A., Zimmer, M.M., Hauri, E.H., Wallace, P.J., 2013. Why do mafic arc magmas contain ~4 wt.% water on average? Earth Planet. Sci. Lett. 364, 168–179. https://doi.org/10.1016/j.epsl.2012.11.044.

Popa, R.-G., Tollan, P., Bachmann, O., Schenker, V., Ellis, B., Allaz, J.M., 2021. Water exsolution in the magma chamber favors effusive eruptions: application of Cl-F partitioning behavior at the Nisyros-Yali volcanic area. Chem. Geol. 570, 120170. https://doi.org/10.1016/j.chemgeo.2021.120170.

Richards, J.P., 2011a. High Sr/Y arc magmas and porphyry Cu-Mo-Au deposits: just add water. Econ. Geol. 106, 1075–1081. https://doi.org/10.2113/econgeo.106.7.1075.

Richards, J.P., 2011b. Magmatic to hydrothermal metal fluxes in convergent and collided margins. Ore Geol. Rev. 40, 1–26.

Richards, J.P., 2018. A shake-up in the porphyry world? Econ. Geol. 113, 1225–1233. https://doi.org/10.5382/econgeo.2018.4589.

Richards, J.P., 2022. Porphyry copper deposit formation in arcs: What are the odds? Geosphere 18, 130–155. https://doi.org/10.1130/GES02086.1.

Richards, J.P., Spell, T., Rameh, E., Razique, A., Fletcher, T., 2012. High Sr/Y magmas reflect arc maturity, high magmatic water content, and porphyry Cu ± Mo ± Au potential: examples from the Tethyan arcs of central and Eastern Iran and Western Pakistan. Econ. Geol. 107, 295–332. https://doi.org/10.2113/econgeo.107.2.295.

Ridolfi, F., Renzulli, A., Puerini, M., 2010. Stability and chemical equilibrium of amphibole in calc-alkaline magmas: an overview, new thermobarometric formulations and application to subduction-related volcanoes. Contrib. Mineral. Petrol. 160, 45–66. https://doi.org/10.1007/s00410-009-0465-7.

Rollinson, H.R., 2014. Using Geochemical Data: Evaluation, Presentation, Interpretation. Routledge.

Schiller, D., Finger, F., 2019. Application of Ti-in-zircon thermometry to granite studies: problems and possible solutions. Contrib. Mineral. Petrol. 174, 51. https://doi.org/10.1007/s00410-019-1585-3.

Shen, T., Wang, G., Bernet, M., Replumaz, A., Ai, K., Song, B., Zhang, K., Zhang, P., 2020. Long-term exhumation history of the Gangdese magmatic arc: Implications for the evolution of the Kailas Basin, western Tibet. Geol. J. 55, 7239–7250. https://doi.org/10.1002/gj.3539.

Shen, Y., Zheng, Y.-C., Hou, Z.-Q., Zhang, A.-P., Huizenga, J.M., Wang, Z.-X., Wang, L., 2021. Petrology of the Machangqing Complex in Southeastern Tibet: Implications for the genesis of potassium-rich adakite-like intrusions in collisional zones. J. Petrol. 62, egab066. https://doi.org/10.1093/petrology/egab066.

Sheng, Y., Jin, S., Lei, L., Dong, H., Zhang, L., Wei, W., Ye, G., Li, B., Lu, Z., 2020. Deep thermal state on the eastern margin of the Lhasa-Gangdese belt and its constraints on tectonic dynamics based on the 3-D electrical model. Tectonophysics 793, 228606. https://doi.org/10.1016/j.tecto.2020.228606.

Signorelli, S., Carroll, M.R., 2000. Solubility and fluid-melt partitioning of Cl in hydrous phonolitic melts. Geochim. Cosmochim. Acta 64, 2851–2862. https://doi.org/10.1016/S0016-7037(00)00386-0.

Sillitoe, R.H., 2010. Porphyry copper systems. Econ. Geol. 105, 3–41. https://doi.org/10.2113/gsecongeo.105.1.3.

Stock, M.J., Humphreys, M.C.S., Smith, V.C., Isaia, R., Brooker, R.A., Pyle, D.M., 2018. Tracking volatile behaviour in sub-volcanic plumbing systems using apatite and glass: insights into pre-eruptive processes at Campi Flegrei, Italy. J. Petrol. 59, 2463–2492. https://doi.org/10.1093/petrology/egy020.

Sun, X., Lu, Y.-J., McCuaig, T.C., Zheng, Y.-Y., Chang, H.-F., Guo, F., Xu, L.-J., 2018. Miocene ultrapotassic, high-Mg dioritic, and adakite-like rocks from Zhunuo in Southern Tibet: implications for mantle metasomatism and porphyry copper mineralization in collisional orogens. J. Petrol. 59, 341–386. https://doi.org/10.1093/petrology/egy028.

Sun, X., Deng, J., Lu, Y., Si, X., Hollings, P., Santosh, M., Li, Q., Zheng, X., 2023b. Two stages of porphyry Cu mineralization at Jiru in the Tibetan collisional orogen: insights from zircon, apatite, and magmatic sulfides. GSA Bull. 135, 2971–2986. https://doi.org/10.1130/B36741.1.

Sun, M., Tang, J.X., Klemd, R., Lin, B., Tang, P., Zhang, Z., Chen, W., Li, F.Q., Qi, J., Chen, H., Gu, F., 2023a. The formation of a giant post-collision porphyry copper system: a case study of the Jiama deposit, Tibet. Geol. Soc. Am. Bull. 136, 1675–1688. https://doi.org/10.1130/B36924.1.

Van den Bleeken, G., Koga, K.T., 2015. Experimentally determined distribution of fluorine and chlorine upon hydrous slab melting, and implications for F–Cl cycling through subduction zones. Geochim. Cosmochim. Acta 171, 353–373. https://doi.org/10.1016/j.gca.2015.09.030.

Wang, R., Richards, J.P., Hou, Z., Yang, Z., DuFrane, S.A., 2014a. Increased magmatic water content-the key to Oligo-Miocene porphyry Cu-Mo Au formation in the Eastern Gangdese Belt, Tibet. Econ. Geol. 109, 1315–1339. https://doi.org/10.2113/econgeo.109.5.1315.

Wang, R., Richards, J.P., Hou, Z.-Q., Yang, Z.-M., Gou, Z.-B., DuFrane, S.A., 2014b. Increasing magmatic oxidation state from Paleocene to Miocene in the Eastern Gangdese Belt, Tibet: implication for collision-related porphyry Cu-Mo Au mineralization. Econ. Geol. 109, 1943–1965. https://doi.org/10.2113/econgeo.109.7.1943.

Wang, X., Sun, M., Weinberg, R.F., Cai, K., Zhao, G., Xia, X., Li, P., Liu, X., 2022. Adakite generation as a result of fluid-fluxed melting at normal lower crustal pressures. Earth Planet. Sci. Lett. 594, 117744. https://doi.org/10.1016/j.epsl.2022.117744.

Wang, R., Weinberg, R.F., Collins, W.J., Richards, J.P., Zhu, D., 2018. Origin of postcollisional magmas and formation of porphyry Cu deposits in southern Tibet. Earth-Sci. Rev. 181, 122–143. https://doi.org/10.1016/j.earscirev.2018.02.019.

Wang, R., Luo, C.-H., Xia, W., He, W., Liu, B., Huang, M.-L., Hou, Z., Zhu, D., 2021. Role of alkaline magmatism in formation of porphyry deposits in Nonarc settings: Gangdese and Sanjiang Metallogenic Belts. SEG Spec. Publ. 22, 205–229. https://doi.org/10.5382/SP.24.12.

Wang, Z., Zheng, Y., Xu, B., Hou, Z., Shen, Y., Zhang, A., Wang, L., Wu, C., Guo, Q., 2024. Mechanisms of fluid degassing in shallow magma chambers control the formation of porphyry deposits. Am. Mineral. https://doi.org/10.2138/am-2023-9091.

Webster, J.D., Piccoli, P.M., 2015. Magmatic apatite: a powerful, yet deceptive, mineral. Elements 11, 177–182. https://doi.org/10.2113/gselements.11.3.177.

Williams-Jones, A.E., Migdisov, A.A. 2014, Experimental Constraints on the Transport and Deposition of Metals in Ore-Forming Hydrothermal Systems, *in* Building Exploration Capability for the 21st Century, Society of Economic Geologists, doi:10.5382/SP.18.05.
Wu, C., Chiaradia, M., Tang, G., Chen, H., 2023. Crustal control on the petrogenesis of adakite-like rocks. Chem. Geol. 632, 121548. https://doi.org/10.1016/j.chemgeo.2023.121548.
Xu, L., Zhu, J., Huang, M., Pan, L., Hu, R., Bi, X., 2023. Genesis of hydrous-oxidized parental magmas for porphyry Cu (Mo, Au) deposits in a postcollisional setting: examples from the Sanjiang region, SW China. Mineral. Deposita 58, 161–196. https://doi.org/10.1007/s00126-022-01143-x.
Yang, Z., Cooke, D.R. 2019. Porphyry Copper Deposits in China. SEG Special Publications, Society of Economic Geologists, 22, 133-187. doi:10.5382/SP.22.05.
Yang, Z.-M., Hou, Z.-Q., White, N.C., Chang, Z., Li, Z., Song, Y., 2009. Geology of the post-collisional porphyry copper–molybdenum deposit at Qulong, Tibet. Ore Geol. Rev. 36, 133–159.
Yang, Z., Hou, Z., Chang, Z., Li, Q., Liu, Y., Qu, H., Sun, M., Xu, B., 2016. Cospatial Eocene and Miocene granitoids from the Jiru Cu deposit in Tibet: petrogenesis and implications for the formation of collisional and postcollisional porphyry Cu systems in continental collision zones. Lithos 245, 243–257. https://doi.org/10.1016/j.lithos.2015.04.002.
Yang, Z.-M., Lu, Y.-J., Hou, Z.-Q., Chang, Z.-S., 2015. High-Mg diorite from Qulong in Southern Tibet: implications for the genesis of adakite-like intrusions and associated porphyry Cu deposits in collisional orogens. J. Petrol. 56, 27.
Yin, A., Harrison, T.M., 2000. Geologic evolution of the Himalayan-Tibetan Orogen. Annu. Rev. Earth Planet. Sci. 28, 211–280. https://doi.org/10.1146/annurev.earth.28.1.211.
Zheng, Y., Zhao, Z., Chen, Y., 2013. Continental subduction channel processes: Plate interface interaction during continental collision. Chin. Sci. Bull. 58, 4371–4377. https://doi.org/10.1007/s11434-013-6066-x.
Zhu, D.-C., Zhao, Z.-D., Niu, Y., Mo, X.-X., Chung, S.-L., Hou, Z.-Q., Wang, L.-Q., Wu, F.-Y., 2011. The Lhasa Terrane: record of a microcontinent and its histories of drift and growth. Earth Planet. Sci. Lett. 301, 241–255. https://doi.org/10.1016/j.epsl.2010.11.005.
Zhu, D.-C., Zhao, Z.-D., Niu, Y., Dilek, Y., Hou, Z.-Q., Mo, X.-X., 2013. The origin and pre-Cenozoic evolution of the Tibetan Plateau. Gondwana Res. 23, 1429–1454. https://doi.org/10.1016/j.gr.2012.02.002.
Zhu, D.-C., Wang, Q., Cawood, P.A., Zhao, Z.-D., Mo, X.-X., 2017. Raising the Gangdese mountains in southern Tibet. J. Geophys Res. Solid Earth 122, 214–223. https://doi.org/10.1002/2016JB013508.
Zhu, D.-C., Wang, Q., Chung, S.-L., Cawood, P.A., Zhao, Z.-D., 2019. Gangdese magmatism in southern Tibet and India–Asia convergence since 120 Ma. Geol. Soc. Lond., SP 483, 583–604. https://doi.org/10.1144/SP483.14.
Zimmer, M.M., Plank, T., Hauri, E.H., Yogodzinski, G.M., Stelling, P., Larsen, J., Singer, B., Jicha, B., Mandeville, C., Nye, C.J., 2010. The role of water in generating the calc-alkaline trend: new volatile data for Aleutian magmas and a new tholeiitic index. J. Petrol. 51, 2411–2444. https://doi.org/10.1093/petrology/egq062.